Tectonophysics xxx (2016) xxx–xxx

Contents lists available at ScienceDirect

Tectonophysics

journal homepage: www.elsevier.com/locate/tecto

Fifteen years of surface deformation in Western Taiwan: Insight from SAR interferometry

Mong-Han Huang [a,b,*], Roland Bürgmann [a,b], Jyr-Ching Hu [c]

[a] Department of Earth and Planetary Science, University of California, Berkeley, CA 94720-4767, USA
[b] Berkeley Seismological Laboratory, University of California, Berkeley, CA 94720-4767, USA
[c] Department of Geosciences, National Taiwan University, Taipei 10617, Taiwan

ARTICLE INFO

Article history:
Received 2 March 2015
Received in revised form 4 January 2016
Accepted 11 February 2016
Available online xxxx

Keywords:
Taiwan
InSAR
Crustal deformation
Land subsidence

ABSTRACT

Geodetically measured surface displacements are produced by a combination of underlying deformation processes acting at different spatial and temporal scales. A complete history of surface measurements in an area can help discriminate contributions from tectonic, hydrologic, and anthropogenic processes. In this study, we use Synthetic Aperture Radar (SAR) images of the active mountain front and adjacent coastal plain of southwestern Taiwan to generate time series of surface deformation from 1995 to 2001 and from 2005 to 2008 based on the InSAR small baseline method. The InSAR measurements agree well with LOS motions estimated from continuous GPS measurements of 3D displacements between 2006 and 2008. A significant range increase in line of sight (LOS) is dominated by land subsidence in the coastal area of western and southwestern Taiwan. Subsidence rates vary with annual periods and are highly correlated with seasonal precipitation, which are likely associated with groundwater recharge and withdrawal. The long-term deformation is dominated by long-term tectonic loading in SW Taiwan during the interseismic period of the earthquake cycle, including elastic strain along or continuous creep on the active faults. Our results show the ability of InSAR to reveal spatiotemporal crustal deformation in western Taiwan with high spatial resolution and accuracy, which is potentially important for evaluating seismic hazards.

1. Introduction

Taiwan is one of the most active tectonic regions in the world driven by the collision of the Eurasian Plate and the Philippine Sea Plate (Fig. 1a). Spatio-temporal variations of displacements at the earth's surface result from fault-related crustal deformation during inter-, co-, and postseismic periods. With help from modern geodesy techniques, it is possible to develop kinematic models to improve our understanding of seismic and aseismic fault slips and to determine the seismic potential of faults (Avouac, 2015). On the other hand, substantial crustal deformation could also be the result of non-tectonic processes. For example, land subsidence due to anthropogenic activities has been a growing concern in western Taiwan (Liu et al., 2004). The pumping of groundwater leads to a drop in hydraulic head levels in aquifers, reduces pore fluid pressure, accelerates compaction of sediments, and results in land subsidence (Schmidt and Bürgmann, 2003). Annual recharge and discharge of groundwater cause the hydraulic head level to rise and fall during wet and dry seasons, respectively. The poroelastic response of the aquifer leads to surface rebound and subsidence that is observable geodetically (e.g. Schmidt and Bürgmann, 2003; Chaussard et al., 2014; Miller and Shirzaei, 2015). On a decadal time scale, tectonic interseismic deformation tends to be steady, whereas periodic and mostly vertical deformation is diagnostic of land subsidence/rebound. As a result, geodetic measurements in space and time could potentially separate tectonic movement from hydraulic activities.

Geodetic measurements including GPS and leveling have provided valuable observations of crustal deformation in Taiwan (Yu et al., 1997; Ching et al., 2007; Hsu et al., 2009; Lin et al., 2010). The GPS network, with stations generally spaced less than 10 km apart, highlights the uplift/subsidence regions as well as a generally NW–SE shortening pattern in Taiwan (Fig. 1b and c). However, these measurements do not provide the high spatial resolution needed to resolve surface creep on individual faults or to accurately constrain the fault locking depth. Synthetic aperture radar interferometry (InSAR) has been used to monitor crustal deformation since the early 1990s. InSAR is a unique tool that provides a high-resolution 2-D image of surface deformation for a target area and has wide applications in studies of earthquake cycles, volcanic deformation, glacier movement, land subsidence, and various other natural and anthropogenic deformation processes (Bürgmann et al., 2000). In western Taiwan, several studies have used InSAR to investigate interseismic crustal deformation (e.g. Fruneau et al., 2001; Huang et al., 2006, 2009; Wu et al., 2013), coseismic surface

* Corresponding author at: Jet Propulsion Laboratory, California Institute of Technology, 4800 Oak Grove Drive, Pasadena, CA 91109, USA. Tel.: +1 818 354 4456.
E-mail address: mong@seismo.berkeley.edu (M.-H. Huang).

http://dx.doi.org/10.1016/j.tecto.2016.02.021
0040-1951/

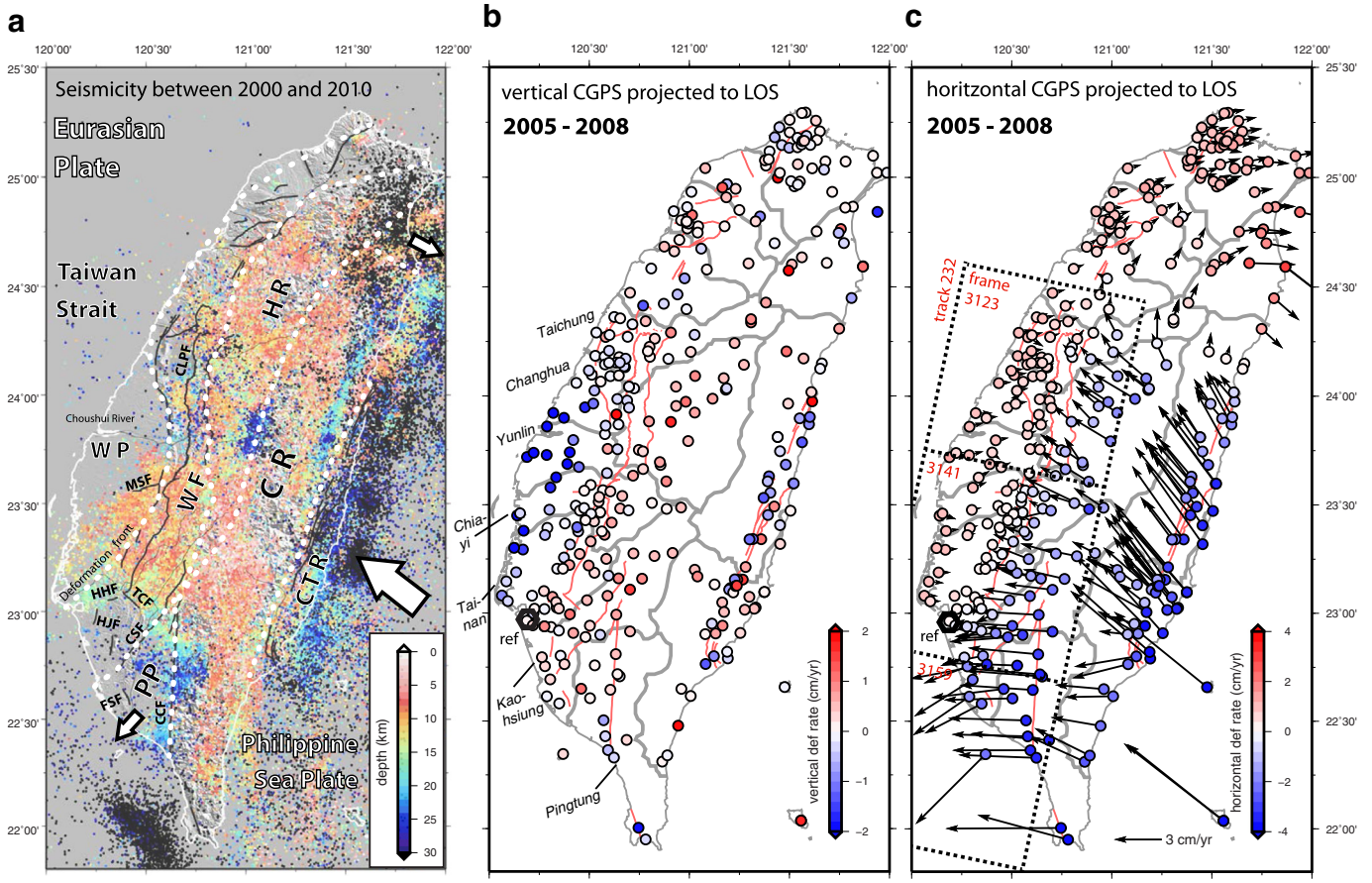

Fig. 1. (a) Seismicity ($M > 1$) distribution in western Taiwan between 2000 and 2010. The color of the dots indicates the depth of seismicity, the black lines are active faults published by Central Geology Survey (CGS), and the white dashed lines are the boundaries of major geologic units in Taiwan. The seismicity data are downloaded from the Taiwan Earthquake Center (TEC). Faults — MSF: Meishan fault; TCF: Tsochen fault; HHF: Hsinhua fault; HJF: Houjiali fault; CSF: Chishan fault; FSF: Fengshan fault; CCF: Chaochou fault; CLPF: Chelungpu fault. Tectonic units — WP: Western Plain; WF: Western Foothills; PP: Pingtung Plain; HR: Hsuehshan Range; CR: Central Range; CTR: Costal Range. (b) Mean vertical velocities projected to SAR satellite look angle based on continuous GPS time series during 2005–2008. (c) Mean annual horizontal velocities projected to the satellite look direction (~N75°W). The hexagon in (b) and (c) is the reference point. The thick gray lines in (b) and (c) are the county boarders in Taiwan. The labels indicate name of the counties mentioned in this study. (For interpretation of the references to color in this figure legend, the reader is referred to the online version of this chapter.)

displacements (e.g. Pathier et al., 2003; Chang et al., 2004; Huang et al., 2013), and land subsidence (e.g. Hung et al., 2010, 2011; Tung and Hu, 2012; Hsieh et al., 2011). These studies only focus on measurements of the mean temporal deformation pattern, and they lack observations of temporal changes, which could provide additional information of longer-term (e.g. decadal) and shorter-term (e.g. seasonal) variations of deformation. In recent years, InSAR methods have been developed to detect stable point scatterers (or persistent scatterers) from interferograms and generate time series of displacement for each point scatterer (Ferretti et al., 2000; Hooper, 2008).

In this study, we process InSAR data spanning western Taiwan including (from north to south) Taichung, Changhua, Yunlin, Chiayi, Tainan, Kaohsiung, and Pingtung counties (see Fig. 1b for location of counties) to reveal crustal deformation in the region at high spatial resolution. We use an InSAR processing method building on a small baseline (SBAS) algorithm (Berardino et al., 2002) to detect stable point scatterers and generate time series of line of sight (LOS) displacements between 1995–2001 and 2005–2008. To validate the accuracy of our InSAR results, we incorporate continuous GPS (CGPS) time series recorded at 144 stations, during 2005–2008 (Fig. 1b and c). We convert the three-component GPS displacement time series into the corresponding InSAR LOS motions, and calculate the mean velocity and the amplitude of seasonal displacement cycles of GPS and InSAR measurements, respectively. With time series analysis, we can further investigate the seasonal surface displacements and find relationships with precipitation, groundwater table (or hydraulic head level) changes, and anthropogenic activities. These non-tectonic deformation processes are different from steady tectonic interseismic motions, surface slip along aseismically creeping faults and earthquake events (e.g. the 1999 M_w 7.6 Chi–Chi earthquake). We aim to separate out short- and long-term deformations based on the high density of point scatterer time series observations. This information is of value for water resource management as well as for natural hazard mitigation in western Taiwan.

2. Geologic setting of Taiwan

The Taiwan Island is the result of oblique collision between the Philippine Sea Plate and the continental margin of the Eurasian Plate (Suppe, 1984). The Philippine Sea Plate is moving northwest at a convergence rate of ~82 mm/yr (Yu et al., 1997; Lin et al., 2010). This two-plate collision gave rise to a series of north–south trending mountain ranges and active fold-and-thrust belts, and also brings about destructive earthquakes (Shyu et al., 2005; Lin et al., 2010; Ching et al., 2011).

Five geologic domains are separated by major boundary fault structures. From west to east, several major NS trending fault zones separate the Coastal Plain, the Western Foothills, the Hsuehshan Range, the Central Range, and the Coastal Range (Fig. 1a). The Coastal Plain is composed of Quaternary alluvial deposits mainly from the Western Foothills and the Central Range. The Western Foothills are composed of shallow marine sediments from the late Oligocene to early Pleistocene (Hsu

Please cite this article as: Huang, M.-H., et al., Fifteen years of surface deformation in Western Taiwan: Insight from SAR interferometry, Tectonophysics (2016), http://dx.doi.org/10.1016/j.tecto.2016.02.021

et al., 2009), which were deformed by north–south trending fold-and-thrust structures since the early Pleistocene (Ho, 1986). The Central Range is the main divide of the river systems in western and eastern Taiwan, and is mainly made of metamorphic units that were rapidly exhumed (~3–5 mm/yr), since the Pliocene (e.g., Fuller et al., 2006).

Based on the relocation of more than 110,000 M_L 1–4 earthquakes in Taiwan, the seismicity indicates an extensive, shallowly east dipping detachment beneath central Taiwan at ~10 km depth (Carena et al., 2002). Several bedding-parallel thrust ramps flatten to this main detachment underneath the Western Foothills and are capable of producing large displacement along the thrust ramps such as in the 1999 M_w 7.6 Chi–Chi earthquake in central Taiwan. In southwestern Taiwan, shallow seismicity extends toward the Tainan coastal area (Fig. 1a). South of this seismic zone, surface fault creep is observed at the eastern margin of the Tainan Tableland that could be due to continuous slip of the Houjiali fault (HJF in Fig. 1a) (Fruneau et al., 2001; Huang et al., 2006, 2009). In southern Taiwan, the Chishan fault (CSF in Fig. 1a) and the Chaochou fault (CCF in Fig. 1a) bound the Pingtung Plain (PP in Fig. 1a) (Hu et al., 2007). The current crustal displacement rate in the Pingtung Plain is ~50 mm/yr southwestward relative to the stable Eurasian Plate (Fig. 1c) (Hu et al., 2007) and is considered to be the result of "tectonic escape" (Lacombe et al., 2001). Surface strain rate and rotation rate analyses (e.g. Ching et al., 2007; Huang et al., 2013) around the Chishan fault support the tectonic escape model. The detachment underneath the Pingtung Plain is generally deeper (>15 km) than that below central Taiwan (10–15 km) (Carena et al., 2002; Suppe personal communication). The 2010 M_w 6.2 Jia-Shien earthquake occurred near the transition between the different detachment depths (Huang et al., 2013).

3. Hydrology and land subsidence in Taiwan

Anthropogenic activities involved with the utilization of groundwater have increased the magnitude of land subsidence since the 1950s (Hsu, 1998; Tung and Hu, 2012). Due to rapid growth of economic demands and population, groundwater over-pumping for agriculture and industrial purpose has been a serious problem in Taiwan for the last four decades. When pumping rates exceed the annual recharge rate, the initial drop of groundwater level to new lows leads to the unrecoverable consolidation of young sedimentary layers, and hence causes rapid land subsidence. During fast artificial groundwater pumping periods, the surface elevation is coupled with the hydraulic head, but following cessation of groundwater pumping, the land surface typically continues to subside for several years due to delayed compaction, even when the hydraulic head recovered back to the pre-pumping level (Chen et al., 2007). Smaller and recoverable surface elevation changes are associated with poroelastic deformation from hydraulic head variations (including annual) at depths above the previously lowest level. Fig. S1 shows the interpolated land subsidence distribution in western Taiwan based on annual leveling surveys, which is also seen in CGPS measurements (Fig. 1b). From north to south, the recent land subsidence rates in the Changhua–Yunlin counties exceeded 8 cm/yr, ~1–3 cm/yr in the Chiayi–Tainan–Kaohsiung counties, and ~1.5 cm/yr in the Pingtung County, during 2002–2006 (Hu et al., 2006; Hsieh et al., 2011).

The Choushui River (Fig. 1a) flows from the Central Range toward the Taiwan Strait, and the area of the 1800 km^2 Choushui River alluvial fan includes most of the Changhua and Yunlin counties. Due to frequent floods and channel migrations, sedimentary layers consist mostly of soft clays and fine sands that have lower strength and permeability than gravels, and coarse sands on the east side of the Coastal Plain (Liu et al., 2004). During 1980–2000, over-pumping of groundwater has induced land subsidence at more than 10 cm/yr in the Choushui river alluvial fan, which covers most of Changhua and Yunlin counties (Tung and Hu, 2012) (Fig. S1). Based on InSAR observations, Tung and Hu (2012) estimated a subsidence rate of more than 70 mm/yr during the 1996–1999 time period in Yunlin County, with the rate staying about the same during 2006–2008 (Hung et al., 2010, 2011).

The Pingtung Plain contains an area of 1210 km^2 in southwestern Taiwan (PP in Fig. 1a). The source of the late Pleistocene and the Holocene unconsolidated sediments is coastal to estuarine sand and mud, with abundant shallow marine to lagoonal shells and foraminifers (Hu et al., 2007). In the Pingtung County, significant land subsidence due to anthropogenic groundwater pumping occurred since the 1960s, with InSAR-measured rates near ~20 cm/yr during 1995–2000 (Hsieh et al., 2011). Other geodetic data such as GPS (Fig. 1b and c) and leveling agree with InSAR measurements, and show dominant subsidence near the coastal area. In contrast, surface uplift is observed in the Western Foothills due to tectonic deformation.

Several borehole layer-compaction monitoring wells were installed in the Western Plain to measure soil and sand consolidation in individual sedimentary layers at different depths. During 1998–2001, the measurements in the Choushui River alluvial fan, reveal a 14–16 cm/yr compaction rate in Changhua County between the land surface and the borehole bottom, and 3–5 cm/yr in Yunlin County with ~1–2 cm rebound between June and August (rainy seasons) every year (Liu et al., 2004). This effect implies that recoverable poroelastic deformation is caused by short-term fluctuations of groundwater level, while the long-term groundwater level drop leads to rapid and irreversible sediment compaction.

4. Data and method

4.1. Data

4.1.1. Continuous GPS network

In western Taiwan, the Ministry of Interior, Central Geological Survey, and Academia Sinica operate a continuous GPS network with about 10 km station spacing in western Taiwan (Ching et al., 2011). In recent years, more than 400 continuous GPS (CGPS) stations were installed in Taiwan and record time series of east–west, north–south, and vertical surface deformation. The CGPS data are maintained and processed by the GPS laboratory in the Institute of Earth Science, Academia Sinica, Taiwan. The details of the data processing and the time series data are available at the website: http://gps.earth.sinica.edu.tw. More than 140 stations with daily position data are located within our SAR acquisition coverage. In order to compare with InSAR results in LOS, a combination of vertical and horizontal components, we project horizontal CGPS displacements onto satellite look direction. Fig. 1b shows the GPS-measured mean vertical velocities relative to a reference station (labeled REF in the figure) in the Tainan tableland, during 2005–2008. Arrows in Fig. 1c show the horizontal velocities and the red-to-blue circles in Fig. 1c show the horizontal N–S and E–W velocities projected into the SAR satellite look direction.

4.1.2. SAR images

We use SAR images from the European Remote Sensing (ERS) 1 & 2 and Envisat satellites developed by the European Space Agency (ESA), both carry C-band (wavelength = 5.67 cm) SAR sensors (Bürgmann et al., 2000) and monitored Earth's surface from 1991 to 2012 (ERS-1: 1991–2000; ERS-2: 1995–2011; Envisat: 2002–2012). In this study, we use totally 40 ERS SAR acquisitions between 1995 and 2001 (Table S1), and 21 Envisat ASAR acquisitions between 2005 and 2008 (Table S2). We focus on descending orbit (north-to-south flyover) acquisitions because they have a higher temporal coverage for western Taiwan. For both ERS and Envisat datasets, acquisitions of track 232 and frames 3123–3159 (Fig. 1b) cover most of western Taiwan, and the satellite look direction is ~N75°W and the average look angle is ~23.5° off vertical. We obtain floating scenes (frames 3123, 3141, and 3159) for the ERS datasets and continuous pass from N22.3° to N24.5° for the Envisat dataset.

Please cite this article as: Huang, M.-H., et al., Fifteen years of surface deformation in Western Taiwan: Insight from SAR interferometry, Tectonophysics (2016), http://dx.doi.org/10.1016/j.tecto.2016.02.021

4.2. InSAR processing methods

For InSAR processing and time series generation, we use the code ROI_PAC 3.0 (Rosen et al., 2004) to produce all of the interferograms. The 90 m Shuttle Radar Topography Mission (SRTM) digital elevation model (DEM) is used to remove the phase due to topography. Snaphu 1.4.2 (Chen and Zebker, 2002) is used for phase unwrapping. Section 6.1 provides a detailed discussion of the phase unwrapping approach. For the Envisat dataset, we additionally perform the phase local oscillator drift correction for each interferogram using the empirical model of Marinkovic and Larsen (2013) following Fattahi and Amelung (2014). Persistent Scatterer InSAR is a method to detect stable point scatterers based on amplitude or coherence from a number of interferograms, and we can carry out the displacement in time of these point scatterers (Ferretti et al., 2000; Berardino et al., 2002). In this study, we generate point scatterers and their time series based on the small baseline subset (SBAS; Berardino et al., 2002) algorithm.

4.2.1. Detecting stable scatterers

The vegetated and topographically rough terrain of Taiwan makes conventional InSAR challenging and motivates the need for improving processing methods. To do this we first process interferograms that have relatively small spatial and temporal baselines. In this study, the spatial baselines are <200 m and the temporal baselines are <2.5 years (Fig. 2), resulting in a total of 110 interferograms processed from 40 ERS acquisitions, and 121 interferograms from 21 Envisat acquisitions. For ERS (Fig. 2a), we include the August 19, 1999 and the September 23, 1999 pair, even the spatial baseline is more than 500 m. This is because this acquisition is only 35 days apart and it is right before and after the M_w 7.6 Chi–Chi earthquake occurred on September 20, 1999. For Envisat (Fig. 2b), we do not include the April 03, 2004 acquisition because there is only one interferogram that can be paired with this acquisition. To detect point scatterers, we estimate coherence of each pixel in every interferogram, and consider pixel coherence higher than a certain threshold value (here we use 0.3) as stable. For spatial phase unwrapping, we only unwrap these stable pixels in order to reduce computation time. If the coherence of an assumed stable pixel is higher than the threshold for more than 50% of all interferograms, we then consider this pixel as a "point scatterer". Different from the typical persistent scatterer algorithms, we do not need to assign a super master acquisition. We instead process interferograms that have small spatial and temporal baselines, which generally have higher coherence and allow for more point scatterer candidates. Note that based on this criterion a point scatterer may not exist throughout all of the interferograms, and therefore we interpolate the phase of this pixel in those interferograms based on nearby points within a few kilometers using the program *griddata* in *Matlab* code. This procedure relies on the condition that the spatial wavelength of the crustal deformation signal is generally greater than tens of kilometers.

Each interferogram contains the phase-change information of each pixel, which provides information about the surface deformation between two acquisitions, but also includes DEM and satellite orbital errors, and other noises. To distinguish surface deformation from noise, we rely on large quantities of interferograms and treat the analysis as an over-determined inverse problem.

4.2.2. Time series processing

An interferogram ($\Delta\Psi_k$) is the phase difference of two acquisitions (Ψ_i and Ψ_j). At a given location (x, y) the phase difference can be represented as,

$$\Delta\Psi_k(x,y) = \Psi(x,y,t_i) - \Psi(x,y,t_j), \quad i \text{ or } j = 1,2,\ldots,N; \quad k = 1,2,\ldots,M. \tag{1}$$

N and M are the total number of acquisitions and interferograms, respectively. The $\Delta\Psi_k(x,y)$ term can be written as,

$$\begin{aligned}\Delta\Psi_k(x,y) = \frac{4\pi}{\lambda}\Big\{ & v(x,y)(t_i - t_j) + \frac{1}{2}a(x,y)\left(t_i^2 - t_j^2\right) + \frac{1}{6}\Delta a(x,y)\left(t_i^3 - t_j^3\right) \\ & + \left[D_i(x,y) - D_j(x,y)\right]\Big\} + \frac{4\pi}{\lambda}\frac{B_{perp,k}}{R_{x,y}\sin\theta_{x,y}}\Delta h(x,y) \\ & + \frac{4\pi}{\lambda}\left[\varepsilon_i(x,y) - \varepsilon_j(x,y)\right] + \alpha_k(x,y)\end{aligned} \tag{2}$$

where $v(x, y)$, $a(x, y)$, and $\Delta a(x, y)$ respectively denote the velocity, acceleration, and acceleration derivative terms and are assumed constant throughout the time series of a given point (x,y). $\Delta h(x, y)$ is the DEM error, $B_{perp,k}$ is the perpendicular spatial baseline (or orbit separation) of interferogram k, $R_{x,y}$ is the distance between target and satellite, $\theta_{x,y}$ is the satellite look angle at (x, y), and λ is the sensor wavelength. The $D(x, y)$ terms represent surface motions that cannot be described by $v(x, y)$, $a(x, y)$, and $\Delta a(x, y)$. The $\varepsilon(x, y)$ terms are the atmosphere-

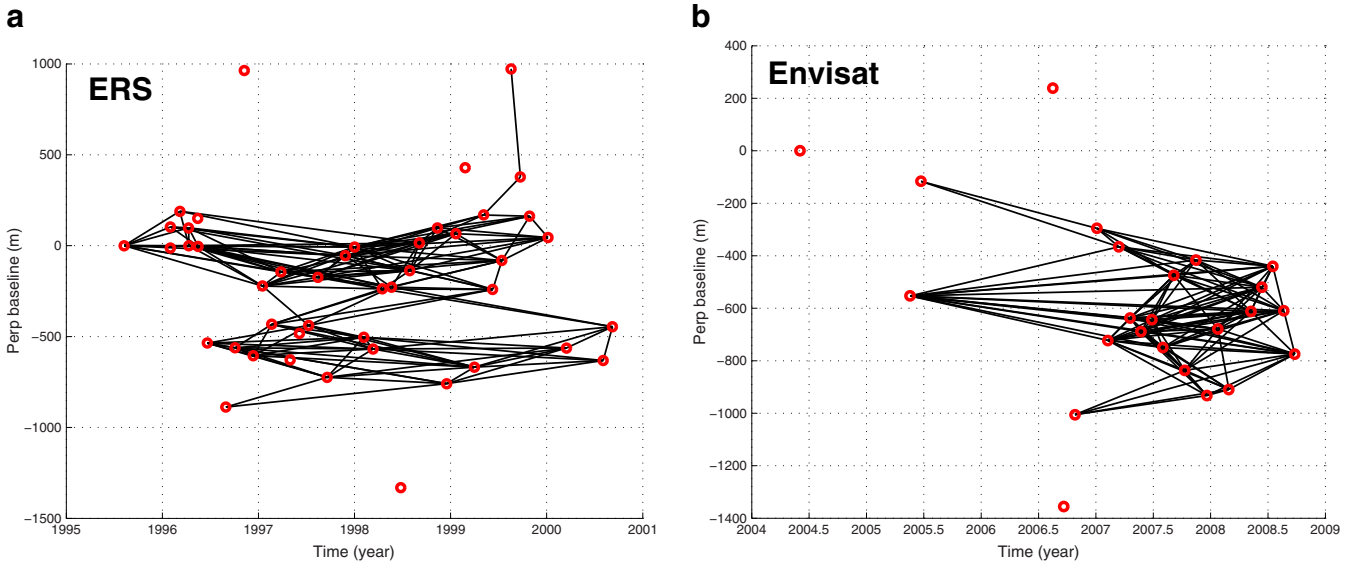

Fig. 2. Baseline of acquisitions relative to the first acquisition for (a) ERS and (b) Envisat. The red dots are individual SAR acquisitions and their relative spatial perpendicular baseline, and the black lines are pairs used for time series inversions. (For interpretation of the references to color in this figure legend, the reader is referred to the online version of this chapter.)

Please cite this article as: Huang, M.-H., et al., Fifteen years of surface deformation in Western Taiwan: Insight from SAR interferometry, Tectonophysics (2016), http://dx.doi.org/10.1016/j.tecto.2016.02.021

related phase of given acquisition (also called "Atmospheric Phase Screen"), and α_k is the remaining model residual.

We can rewrite Eq. (2) in a matrix representation as

$$\Delta\Psi_k(x,y) = \mathbf{MN} + \alpha_k(x,y), \tag{3}$$

with

$$\mathbf{M} = \frac{4\pi}{\lambda}\begin{bmatrix} -1 & 1 & 0 & \dots & t_1-t_2 & \frac{t_1^2-t_2^2}{2} & \frac{t_1^3-t_2^3}{2} & \frac{B_{perp,1}}{R_{x,y}\sin\theta_{x,y}} \\ -1 & 0 & 1 & \dots & t_1-t_3 & \frac{t_1^2-t_3^2}{2} & \frac{t_1^3-t_3^3}{2} & \frac{B_{perp,2}}{R_{x,y}\sin\theta_{x,y}} \\ 0 & -1 & 1 & \dots & t_2-t_3 & \frac{t_2^2-t_3^2}{2} & \frac{t_2^3-t_3^3}{6} & \frac{B_{perp,3}}{R_{x,y}\sin\theta_{x,y}} \\ \dots & \dots & \dots & \dots & \dots & \dots & \dots & \dots \\ 0 & 0 & 0 & \dots & t_i-t_j & \frac{t_i^2-t_j^2}{2} & \frac{t_i^3-t_j^3}{6} & \frac{B_{perp,M}}{R_{x,y}\sin\theta_{x,y}} \end{bmatrix},$$

$$\mathbf{N} = \begin{bmatrix} D(x,y,t_1)+\varepsilon(x,y,t_1) \\ D(x,y,t_2)+\varepsilon(x,y,t_2) \\ D(x,y,t_3)+\varepsilon(x,y,t_3) \\ \dots \\ D(x,y,t_N)+\varepsilon(x,y,t_N) \\ v(x,y) \\ a(x,y) \\ \Delta a(x,y) \\ \Delta h(x,y) \end{bmatrix}. \tag{4}$$

Here **M** stores the known information including the pair index, time difference between acquisitions, and spatial baseline related coefficients. The −1, 1, and 0 terms are the pair permutations, and −1 or 1 represents the master or the slave acquisition, respectively. **N** stores the unknown information including parameters v, a, Δa, and Δh. The D terms are the deformation adjustments of each pixel for each acquisition, and the ε terms denote the atmospheric related phases of each pixel for each acquisition. For a case of 50 acquisitions and 400 interferograms, **M** would be a 400×54 matrix, and **N** would be a 54×1 matrix. **M** in Eq. (3) becomes over-determined when $\mathbf{M} > \mathbf{N} + 4$, but **N** cannot be solved simply by using least squares because **M** is too sparse. We instead use the singular value decomposition (SVD) method to solve for matrix **N** (Menke, 1989). As a result, the time series of a stable point (x,y) is described by,

$$U(x,y,t_i) = v(x,y)t_i + \frac{1}{2}a(x,y)t_i^2 + \frac{1}{6}\Delta a(x,y)t_i^3 + D_i(x,y), i = 1\dots\mathbf{N}. \tag{5}$$

Note that the non-modeled $D(x,y,t_i)$ and $\varepsilon(x,y,t_i)$ terms in each acquisition in Eq. (4) cannot be separated directly, but $\varepsilon(x,y,t_i)$ is commonly estimated by applying a high-pass filter in the temporal domain, after applying spatial low-pass filter to individual interferograms. This is because of the assumption that the atmospheric contribution to phase is a random function in time but has long spatial wavelength in each interferogram (Berardino et al., 2002; Mora et al., 2003). We apply a 100×100 m^2 moving window as a low-pass filter to each interferogram, and then a 1-pole high-pass filter in time series with time constant of 2-acquisition interval (70 days) to estimate $\varepsilon(x,y,t_i)$ as well as $D(x,y,t_i)$.

To estimate the seasonality and the mean velocity from the time series (Eq. (5)), we can rewrite Eq. (5) as:

$$U(x,y,t_i) = \bar{v}(x,y)t_i + a(x,y)\sin(2\pi t_i) + b(x,y)\cos(2\pi t_i) + \sigma(x,y,t_i), \tag{6}$$

where a and b are constants that describe the coefficients of the sine/cosine functions at location (x, y), and σ is the remaining unfitted term at t_i. $\bar{v}(x,y)$ is a linear rate fit to the time series in U that represent mean velocity in the time series. Note that $v(x,y)$ in Eq. (5) is a linear coefficient of a third-order polynomial equation, and is different from $\bar{v}(x,y)$ in Eq. (6) that represents the mean velocity of the entire time series. Eq. (6) can be rewritten as.

$$\mathbf{d} = \mathbf{G}\ \mathbf{m} + \sigma, \tag{7}$$

where

$$\mathbf{d} = \begin{bmatrix} D(x,y,t_1) \\ D(x,y,t_2) \\ \dots \\ D(x,y,t_N) \end{bmatrix} \mathbf{G} = \begin{bmatrix} t_1 & \sin(2\pi t_1) & \cos(2\pi t_1) \\ t_2 & \sin(2\pi t_2) & \cos(2\pi t_2) \\ \dots & \dots & \\ t_N & \sin(2\pi t_N) & \cos(2\pi t_N) \end{bmatrix},$$

$$\mathbf{m} = \begin{bmatrix} \bar{v}(x,y) \\ a(x,y) \\ b(x,y) \end{bmatrix}, \text{ and } \sigma = \begin{bmatrix} \sigma(x,y,t_1) \\ \sigma(x,y,t_2) \\ \dots \\ \sigma(x,y,t_N) \end{bmatrix}. \tag{8}$$

We can use least square to solve for $\bar{v}$, a and b for point (x,y), i.e.,

$$\mathbf{m}^{\mathbf{est}}(\bar{v},a,b) = \left(\mathbf{G}^{\mathrm{T}}\mathbf{G}\right)^{-1}\mathbf{G}^{\mathrm{T}}\mathbf{d}, \tag{9}$$

where $\mathbf{G}^{\mathrm{T}}$ is the transpose matrix of **G** and $(\bullet)^{-1}$ is the inverse matrix. The amplitude of the seasonal effect is $(a^2 + b^2)^{1/2}$, and the phase shift (i.e., time of year of the peak seasonal uplift) is $(365 / \pi) \times tan^{-1}(a / b)$.

5. Result

We process ERS (1995–2001) and Envisat (2005–2008) datasets separately due to a data gap during 2001–2004. We then generate time series for ERS and Envisat datasets, and the mean velocity and seasonality for each dataset using the method described in Section 4.2.2. Due to the M_w 7.6 Chi–Chi earthquake in central Taiwan on September 20, 1999, the mean velocity and mean seasonality estimations for frame 3123 are based on results from 1995 to right before the Chi–Chi earthquake. In this section we first investigate the spatial LOS deformation patterns during 1995–2001 and 2005–2008, and then the time series in different regions.

5.1. LOS velocity patterns in two different time periods

Fig. 3a shows the mean LOS surface velocity of western Taiwan during 1995–2001 and Fig. 3b for the 2005–2008 time period. The warm and cold colors in Fig. 3 represent range decrease and increase, respectively. The circles in Fig. 3b are continuous GPS stations with color representing their mean velocity from 3D components projected into the LOS direction using the equation,

$$U_{\mathrm{LOS}} = (U_E\cos\ \phi + U_N\sin\ \phi)\ \ \sin\theta + Uz\ \ \cos\theta, \tag{10}$$

where U_{LOS} is displacement in LOS, and U_E, U_N, and U_Z are GPS displacement in E–W, N–S, and vertical components, respectively. θ is the satellite look angle (19°–27° for ERS and Envisat) and ϕ is the satellite heading direction. For the descending orbit geometry, range increase is due to surface subsidence and/or westward movement; range decrease is due to surface uplift and/or eastward movement. For both the ERS and Envisat datasets, most of the coherent point scatterers are in the Western Plain, especially at locations with higher density of construction. In the Changhua and Yunlin Counties, scatterers are more sparse and unwrapping becomes more challenging here.

During 1995–2001 (Fig. 3a), significant land-subsidence related range increase occurs in the coastal areas, especially in Changhua, Yunlin, Chiayi, and Pingtung counties. On the other hand, range decrease is observed near Meishan, Tainan, and part of the Western Foothills. The velocities in the LOS direction solely derived from the horizontal GPS velocities show a smooth gradient in range-change rate (Fig. 1c) from west to east that has a different pattern from the InSAR result, so we interpret that the range decrease here relates to

Please cite this article as: Huang, M.-H., et al., Fifteen years of surface deformation in Western Taiwan: Insight from SAR interferometry, Tectonophysics (2016), http://dx.doi.org/10.1016/j.tecto.2016.02.021

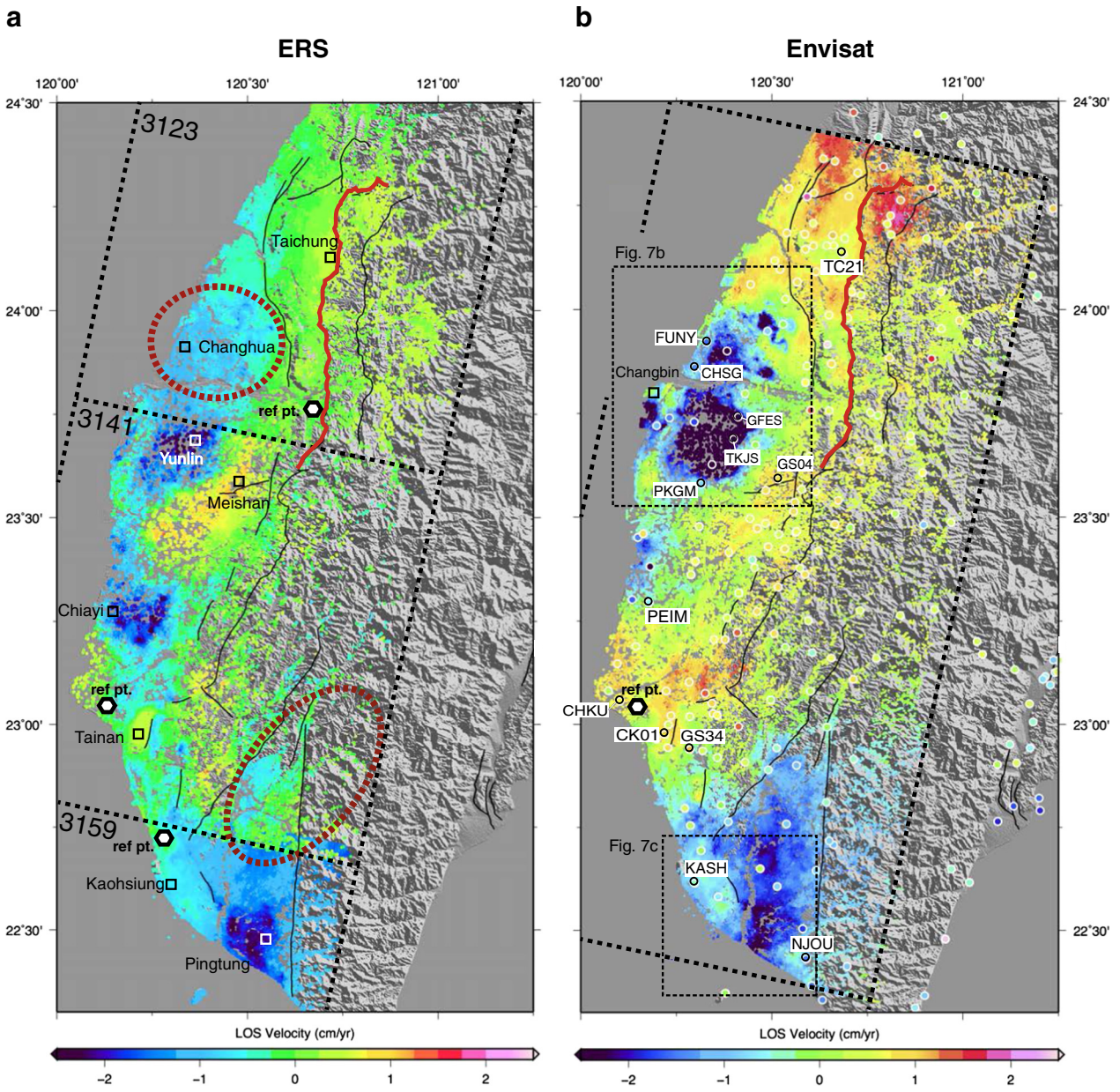

Fig. 3. (a) Mean annual line of sight (LOS) velocity during 1995–1999 (before the 1999 M_w 7.6 Chi–Chi earthquake; frame 3123) or 1995–2001 (frames 3141 and 3159). Positive LOS velocity means range decrease and negative means increase. The red circles highlight areas with significant phase unwrapping errors due to sparse stable points (see Section 6.1 for discussion of phase unwrapping errors). (b) Mean annual LOS velocity during 2005–2008. The circles are continuous GPS (CGPS) stations and the color in the circles indicates the CGPS derived LOS velocity in the same time period as InSAR. (For interpretation of the references to color in this figure legend, the reader is referred to the online version of this chapter.)

tectonic surface uplift (Fig. 1b). In the northern Pingtung Plain, there is a deformation discontinuity between frames 3141 and 3159 possibly due to phase unwrapping error in frame 3141. This unwrapping error is mainly due to fewer point scatterers along the Chishan fault (CSF in Fig. 1a) that does not provide enough connecting points to unwrap northern Pingtung Plain correctly relative to Western Plain. During 2005–2008 (Fig. 3b), the distribution of point scatterers is similar to 1995–2001, but more point scatterers are detected on the Choushui River alluvial fans in the Changhua and Yunlin counties (see Fig. 1b for locations). The crustal deformation pattern is similar to the 1995–2001 periods, but there is a higher range decrease near Taichung City and between the Meishan fault and the Tsochen fault (TCF in Fig. 1a). In addition, the deformation pattern in the Tainan Tableland has changed from uplift in the tableland during 1995–2001 to higher uplift rate east of the Houjiali Fault (see Fig. 1a for locations).

For frame 3123 we exclude the effect of the M_w 7.6 Chi–Chi earthquake (Sep 20, 1999) by considering only data up to the event. In Taichung County, there is no significant surface deformation before the Chi–Chi earthquake and ~30 cm coseismic displacement from Changhua coastal area to Taichung city (Pathier et al., 2003). In the Choushui River alluvial fans, the spatial pattern of the InSAR-based land subsidence area is in agreement with published land subsidence areas derived from leveling measurements by the Water Resource Agency, Department of Economics in Taiwan (Fig. S1). The land subsidence rate in Changhua County is about 10 mm/yr during 1995–1999 and more than 20 mm/yr during 2005–2008. However, the subsidence rate during 1995–1999 may be underestimated compared with leveling measurements (Fig. S1) because of phase unwrapping errors on low density of scatterers. In Yunlin County, the subsidence rate in both 1995–2001 and 2005–2008 periods is more than 20 mm/yr, but the area of land subsidence seems to be larger during 2005–2008. In

Please cite this article as: Huang, M.-H., et al., Fifteen years of surface deformation in Western Taiwan: Insight from SAR interferometry, Tectonophysics (2016), http://dx.doi.org/10.1016/j.tecto.2016.02.021

addition, the southern part of the Changbin industrial area (Fig. 3b), which was built on manmade fill in the early 1990s, has more than 25 mm/yr subsidence rate since 2005.

In Chiayi County, there is a decrease of land subsidence rate from ~25 mm/yr during 1995–2001 to ~10 mm/yr during 2005–2008, and the subsidence area is limited to the coastal area north of Chiayi. East of the land subsidence area, there is 5–15 mm/yr surface uplift between the Meishan fault (MSF in Fig. 1a) and the Tsochen fault (TCF in Fig. 1a) detected by InSAR and CGPS, and the area of uplift roughly outlines the shallow seismicity zone in the Western Foothills (Fig. 1a). The surface uplift rate is slightly lower in the 2005–2008 periods.

In Tainan, there is no significant land subsidence in the coastal area. In the Western Foothills there is 5–10 mm/yr surface uplift near the Tsochen fault. North of the Hsinhua fault (HHF in Fig. 1a), the surface uplift rate is 5–15 mm/yr higher during 2005–2008 than during 1995–2001. In Tainan, the uplift pattern is similar to the topographic expression of the tableland during 1995–2001, and there is land subsidence east of the Houjiali Fault (HJF in Fig. 1a). This result agrees with previous studies (e.g. Fruneau et al., 2001; Huang et al., 2006, 2009) and long-term geologic rate (Chen and Liu, 2000). However, in the 2005–2008 period the surface uplift extends to east of the Houjiali Fault, and the LOS velocity is even higher than in the tableland.

In Kaohsiung and Pingtung, the LOS range increase is mainly due to horizontal motion (Fig. 1c), and the discontinuity between frames 3141 and 3159 during 1995–2001 is due to phase unwrapping errors (the red dotted circle near frame 3159 in Fig. 3a; see Section 6.1 for more detail). In southern Pingtung, there is a higher range increase rate (>20 mm/yr) in both periods related to land subsidence (Fig. 1a). There is a change of surface deformation pattern across the Chishan Fault (CSF in Fig. 1a) and the Fengshan fault (FSF in Fig. 1a).

5.2. Seasonal deformation

Following Section 4.2.2, we calculate the seasonality of western Taiwan during 1995–2001 (1995–1999 for frame 3123) (Fig. 4a) and 2005–2008 (Fig. 4b). To calculate the amplitude of seasonality we

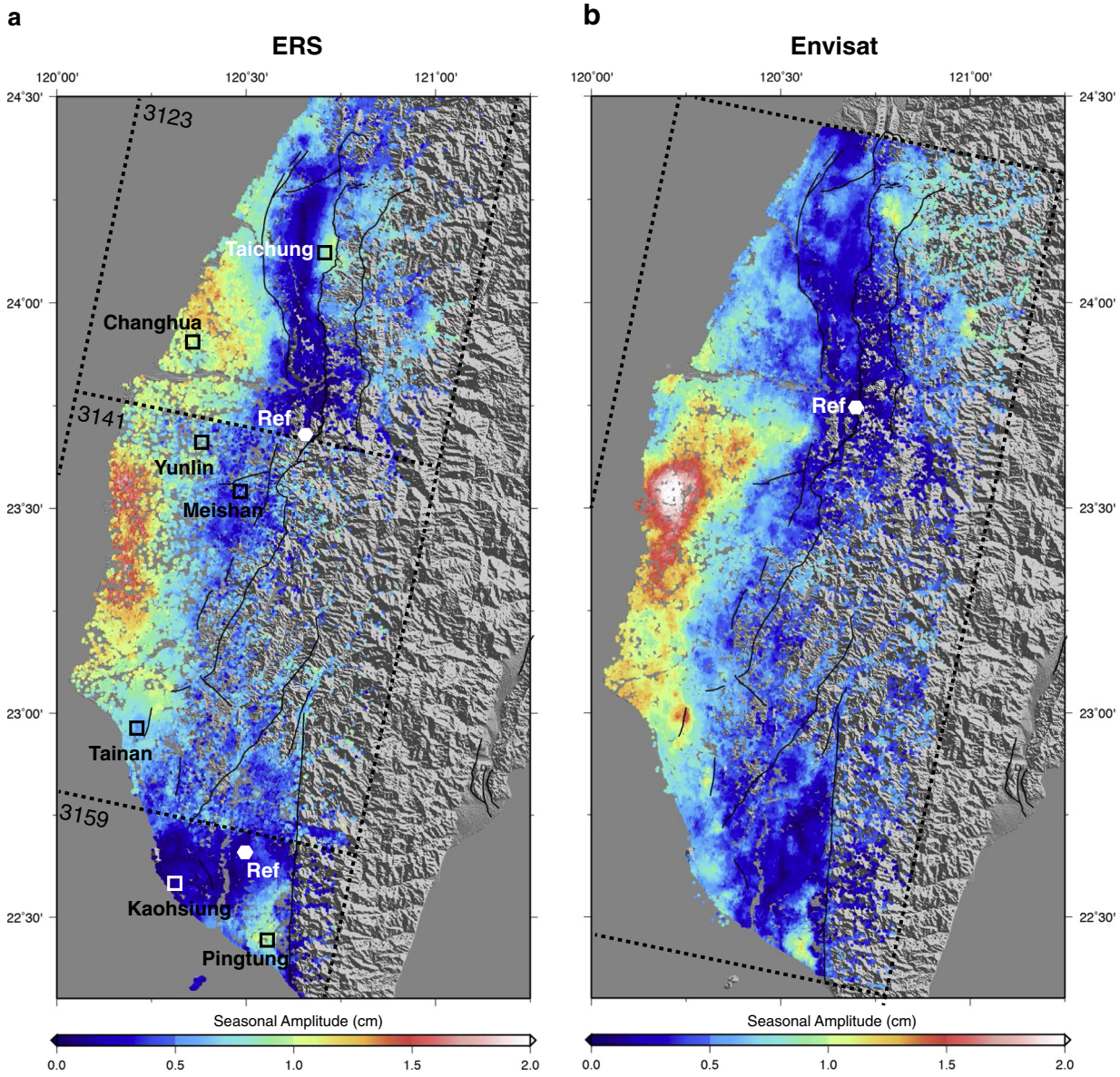

Fig. 4. Mean seasonal variation of western Taiwan during (a) 1995–1999 (before Chi–Chi earthquake frame: 3123) or 1995–2001 (frames 3141 and 3159) and (b) 2005–2008. Yellow-to-red dots indicate higher seasonality. The white hexagons are the reference points. There are three reference points for the ERS dataset due to three separate frames, and the reference point is co-located for frames 3123 and 3141. The reference point is the same for frames 3123 and 3141 in (a). Note the areas with higher seasonality correlate with area experiencing higher land subsidence (Fig. 3). (For interpretation of the references to color in this figure legend, the reader is referred to the online version of this chapter.)

Please cite this article as: Huang, M.-H., et al., Fifteen years of surface deformation in Western Taiwan: Insight from SAR interferometry, Tectonophysics (2016), http://dx.doi.org/10.1016/j.tecto.2016.02.021

choose reference points near GPS stations with minimal seasonal variations that are located in mountainous areas. For the 1995–2001 (ERS) periods we process three frames independently so need three individual reference points (Fig. 4a), whereas only one reference point needed for the 2005–2008 (Envisat) periods (Fig. 4b). During 1995–2001 (Fig. 4a), there is a high seasonal variation in the coastal area, especially in the costal Changhua, Yunlin, Chiayi, and Pingtung counties. The highest amplitude (~15 mm) is along the coast between Yunlin and Chiayi. The seasonal variation in Tainan and Kaohsiung is relatively lower, and becomes higher again in southern Pingtung Plain. There is also higher seasonality in eastern Taichung. During 2005–2008 (Fig. 4b), the seasonality amplitude distribution is similar with the 1995–2001 periods, and the peak amplitude is on the northwestern coast of Chiayi County. In the Tainan Tableland, the seasonality in 2005–2009 is 5–10 mm higher than during the 1995–2001 period.

In general, the areas with a high seasonal variation correspond to areas with significant land subsidence (blue color in Figs. 1b, 3, and S1), such as western Changhua, Yunlin, Chiayi, northwestern Tainan, and southern Pingtung Plain. In the Pingtung Plain (Fig. 3), an area with >15 mm/yr range increase does not correspond to high amplitude of seasonality, as it is associated with the southwestward tectonic escape expressed in horizontal motions (Hu et al., 2007).

5.3. Comparison with CGPS

We project three-component CGPS data into LOS to verify our InSAR result. We choose a period from 2005 through the end of 2008 because it is the period of continuous InSAR records overlapping with CGPS measurements as shown in Figs. 5, 6, and 7. Before calculating GPS LOS velocity we examine every GPS time series, and adjust occasional offsets in the records that appear to be due to GPS antenna adjustments. We use Eqs. (6)–(9) to extract the three components of CGPS velocities from the time series, and then convert three-component velocities into LOS velocity using Eq. (10). With considering station CHKU (Fig. 3b) close to the InSAR reference point as the GPS reference point, we pick an InSAR point closest and within 5 km distance from 144 CGPS stations for comparison. Fig. 5a shows InSAR and CGPS mean LOS velocities at the same locations. This result shows InSAR = 0.87 × CGPS, and R^2 = 0.77.

Fig. 5b and c shows close-ups of Fig. 3b with relevant color scales for the land subsidence areas in Changhua–Yunlin and Pingtung, respectively. Our InSAR result agrees well with the CGPS measurements, and additionally InSAR can further characterize the land subsidence spatial distribution and the subsiding area. For example, in Fig. 5b our InSAR result reveals land subsidence in the regions without GPS station coverage such as western Yunlin (Mailiao industrial area), which was developed on landfill since the late 1990s. In Fig. 5c the area with highest land subsidence rate is in the Linbian town with subsidence rate as −40 mm/yr.

5.4. Time series

Eq. (5) describes the displacement of each stable point at each acquisition time, and thus we can plot its time series. Here we adopt a 100 × 100 m spatial moving window for a low-pass filter and a temporal high-pass filter estimate phase to estimate atmospheric phase screen (ε terms in Eqs. (2) and (4)). However, introducing a temporal high-pass filter could in fact affect real signals in high temporal frequency such as earthquake events, and therefore in the time series plots (Figs. 6 and 7) we present displacement before and after applying the low-pass filter in blue and red dots, respectively.

Fig. 6 shows time series from selected regions with land subsidence in western Taiwan including (from north to south) Changhua, Yunlin, Chiayi, and Pingtung during 1995–2001 and 2005–2008 (see Fig. 3a for locations near four CGPS stations in these areas and the reference points). The mean velocity of the time series is based on the $\bar{v}(x,y)$ term in Eq. (6). Generally, areas undergoing land subsidence in 1995–2001 still show subsidence during 2005–2008. In Changhua County, there is an accumulated subsidence up to 90 mm during 1995–1999. In 2005, the InSAR time series shows LOS displacement lower than GPS projected LOS displacement that could be due to temporal phase unwrapping error of the two acquisitions from the denser network between late 2006 and 2008 as well as lower density of scatterers in Changhua (Fig. 5b). In Yunlin area, the higher density of scatterers reduces phase unwrapping errors. During 1995–2001, the subsidence rate in the Yunlin region is ~30 mm/yr, and >50 mm/yr during 2005–2008. The subsidence rate during 1995–2001 based on our method is less than that of Tung and Hu (2012) (~50 mm/yr during 1996–1999)

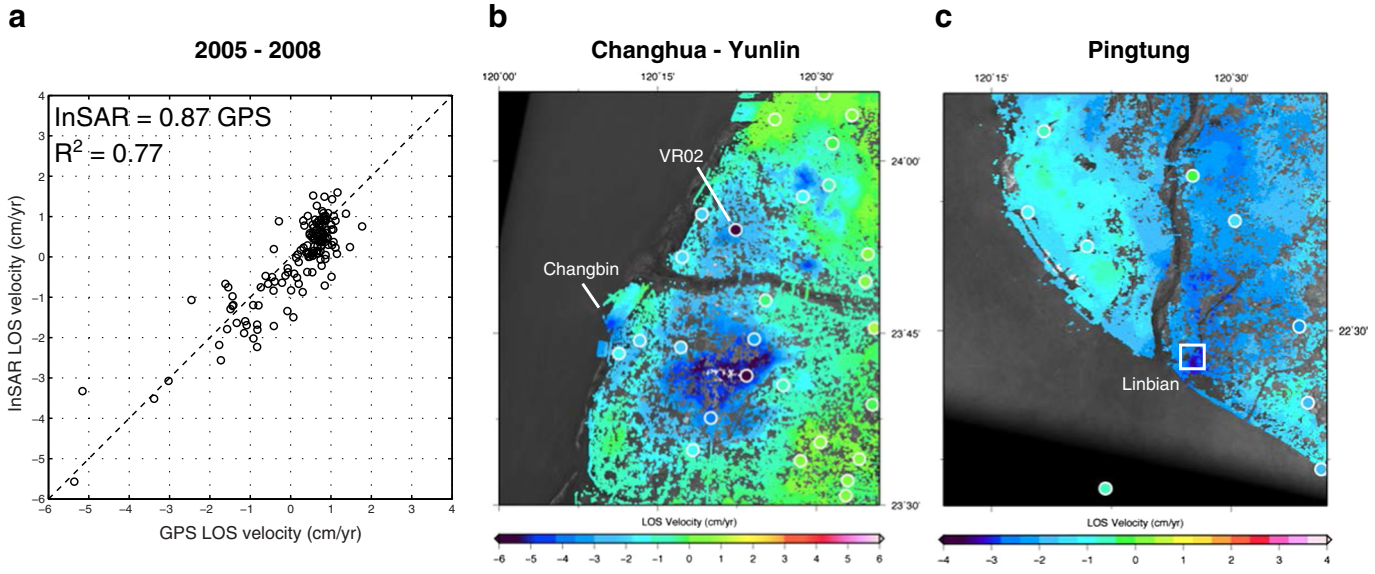

Fig. 5. (a) Comparison of InSAR and CGPS-derived LOS velocities during 2005–2008. The dashed black line represents the one-to-one function. (b) Close-up of Fig. 3b showing land subsidence in western Taiwan (Changhua and Yunlin) and (c) Pingtung Plain. (For interpretation of the references to color in this figure, the reader is referred to the online version of this chapter.)

Please cite this article as: Huang, M.-H., et al., Fifteen years of surface deformation in Western Taiwan: Insight from SAR interferometry, Tectonophysics (2016), http://dx.doi.org/10.1016/j.tecto.2016.02.021

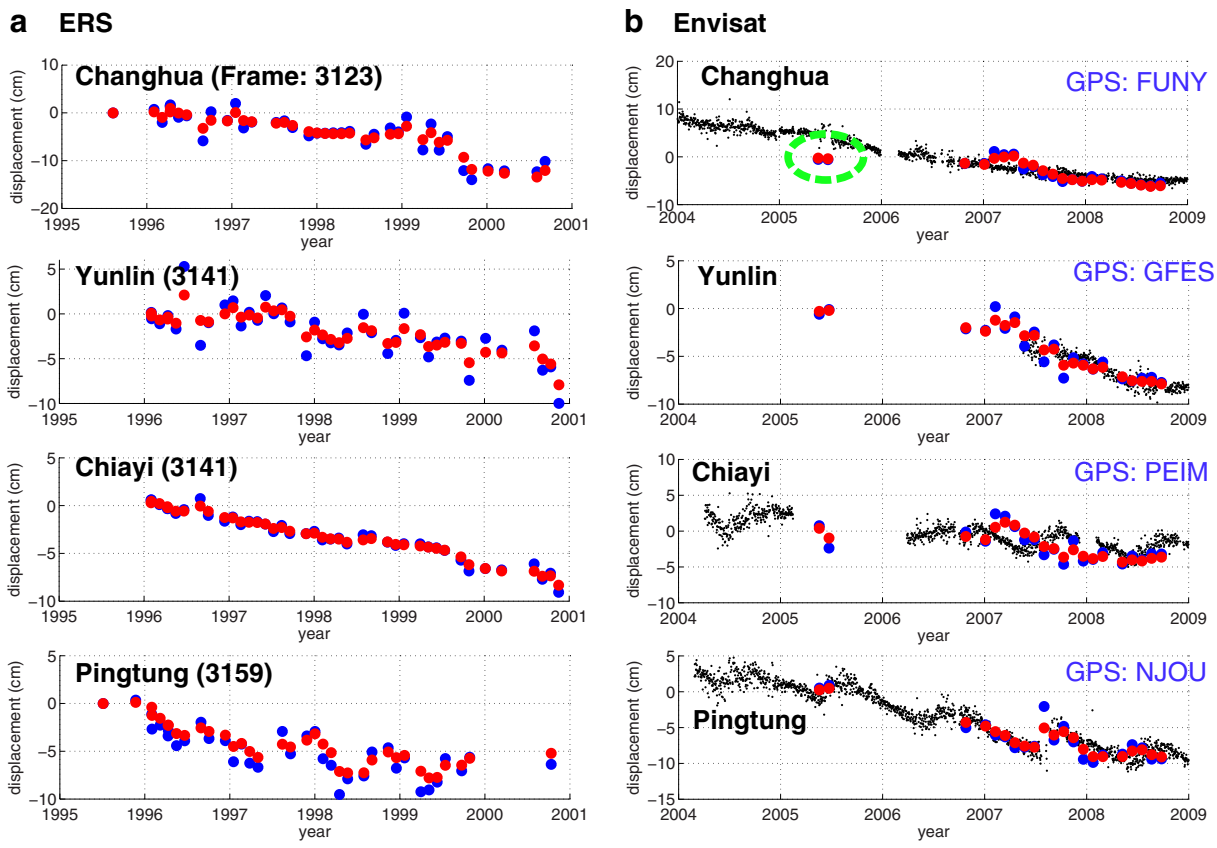

Fig. 6. Selected time series in (from north to south) Changhua, Yunlin, Chiayi, and Pingtung during (a) 1995–2001 and (b) 2005–2008. The blue and red dots are InSAR time series before and after applying a low-pass filter, respectively. The black dots in (b) are CGPS time series (See Fig. 3b for location of stations). Note the time series for ERS (1995–2001) processed separately in different frames (3123, 3141, and 3159) and the Envisat (2005–2009) as a continuous frame, so the temporal sampling is different in different frames. The M_w 7.6 Chi–Chi earthquake occurred in September 1999 near Taichung City. The green circle in (b) indicates possible phase unwrapping errors due to fewer acquisitions during 2004–2006 (see Section 6.1 for discussion of phase unwrapping error). (For interpretation of the references to color in this figure legend, the reader is referred to the online version of this chapter.)

as well as leveling measurements during 2000–2008 (Chen et al., 2011). In the Chiayi coastal area, the subsidence rate is ~25 mm/yr during 1995–2001 and ~10 mm/yr during 2005–2008. From Fig. 3a and b we can find a shift of the subsiding area further toward north. In the Pingtung area, where land subsidence has been a problem for a long time (Hsieh et al., 2011), the subsidence rate is ~20 mm/yr during 1995–2001 and ~25 mm/yr during 2005–2008. There is also a higher seasonal variation (southern Pingtung Plain) in the time series, with seasonal amplitudes that are up to 10 mm during 1995–2001 and ~13 mm during 2005–2008.

Fig. 7 shows time series for points in four regions that experience surface uplift we infer to be of tectonic origin in (from north to south) Taichung, Meishan, Tainan, and Kaohsiung (see Fig. 3a for locations). In the Taichung area, there is a significant seasonal variation during 1995–1999 and the area exhibits uplift and subsidence during summers and winters. The 1999 M_w 7.6 Chi–Chi earthquake produced ~20 cm coseismic LOS displacement in Taichung city (Fig. 6a). In Meishan, the surface uplift (or range decrease) rate is ~6 mm/yr during 1995–2001 and ~4 mm/yr during 2005–2008. The CGPS (S103) time series roughly agrees with InSAR result, but the temporal variation in the CGPS data is less significant. In the Tainan tableland, the surface uplift rate is ~6 mm/yr during 1995–2001 and 2005–2008. The uplift rate is relatively stable and roughly agrees with that observed at the CGPS station CK01 (Fig. 3b) during 2005–2008. The uplift rate estimated here is much lower than found in previous studies (e.g. Huang et al., 2006, 2009, Wu et al., 2013), which selected the reference point in the land subsidence area. Once accounting for different reference points the uplift rates are consistent with previous studies. The surface uplift rate in Kaohsiung is ~5 mm/yr during 1995–2001 and ~−9 mm/yr during 2005–2008, and the subsidence rate during 2005–2008 agrees with the CGPS station KASH.

6. Discussion

6.1. InSAR uncertainties and phase unwrapping error

Although most of the selected point scatterers compare well with GPS measurements (Fig. 5), the remaining spatial and temporal phase unwrapping errors are evident in the mean velocity map for the ERS dataset (Fig. 3a) and in the 2005–2006 time series (e.g. Changhua and Yunlin in Fig. 6b). In this section we present the detail of phase unwrapping strategy of individual interferogram and in the time series process, and we discuss the possible cause of phase unwrapping errors.

For individual interferogram, we first identify pixels with higher coherence (>0.3) as potential stable point scatterers, and then we use a Delaunay triangulation-based nearest neighbor interpolation algorithm to estimate phase value of every pixel. In this algorithm, the phase of an interpolated pixel always assumes the value from its nearest neighbor instead of mean value of neighbor pixels. In this way the phase discontinuity is preserved when an interpolated pixel is surrounded by scatterers with phase values close to zero or 2π. We then unwrap the phase of an interferogram by using the algorithm based on the solution of a minimum cost flow (MCF) network developed by Chen and Zebker (2002). After phase unwrapping we disregard the interpolated points,

Please cite this article as: Huang, M.-H., et al., Fifteen years of surface deformation in Western Taiwan: Insight from SAR interferometry, Tectonophysics (2016), http://dx.doi.org/10.1016/j.tecto.2016.02.021

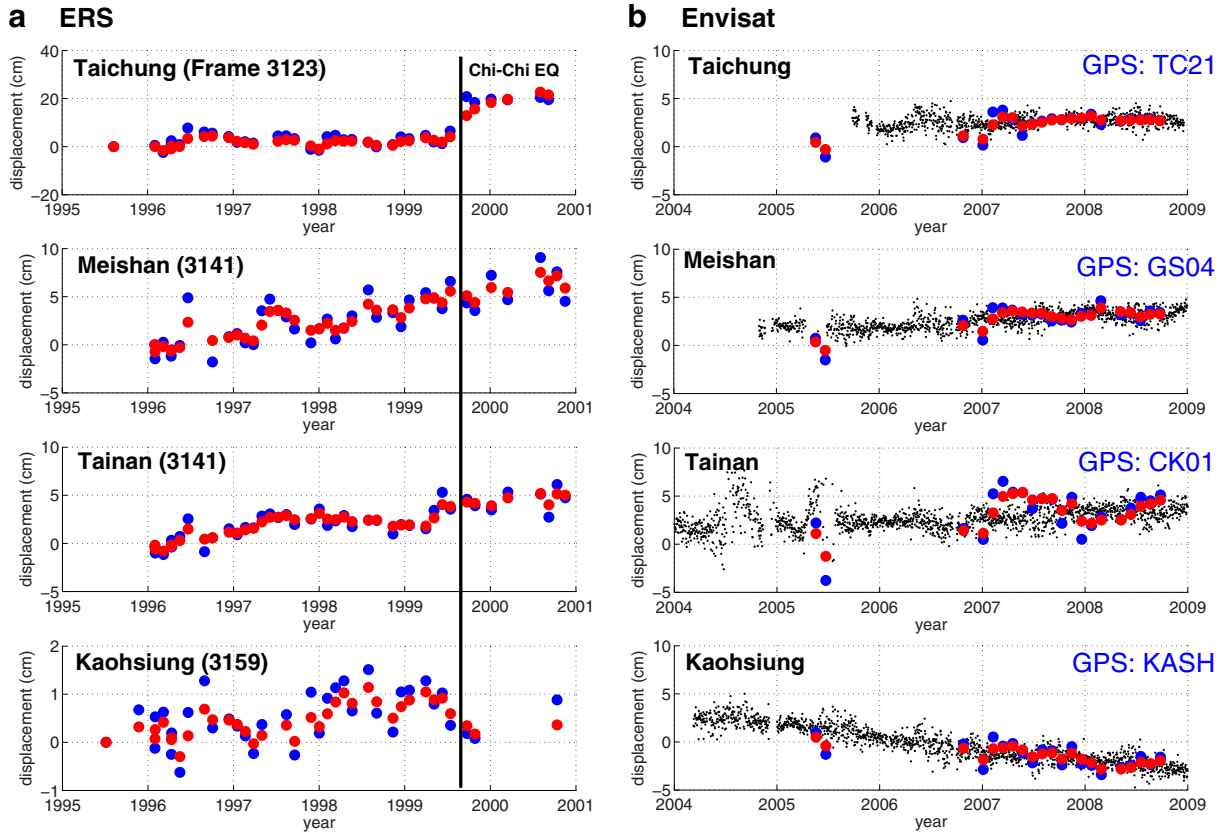

Fig. 7. Selected time series in (from north to south) Taichung, Meishan, Tainan, and Kaohsiung during (a) 1995–2001 and (b) 2005–2008. The blue and red dots are InSAR time series before and after applying a low-pass filter, respectively. The black dots in (b) are CGPS time series (See Fig. 3b for location of stations). Note time series for ERS (1995–2001) dataset is processed in different frames (3123, 3141, and 3159), so the temporal sampling is different in different frames. The M_w 7.6 Chi–Chi earthquake occurred in September 1999 near Taichung City. (For interpretation of the references to color in this figure legend, the reader is referred to the online version of this chapter.)

and only keep the potential stable point scatterers (coherence >0.3) in the interferogram. Eventually we consider a point as a stable scatterer only if the coherence of this point is >0.3 at least in 50% of all interferograms.

This strategy could miscalculate cycles of phase unwrapping if [1] an isolated point scatter (or a cluster of scatterers) is too far away from its neighbor scatterers, [2] if there is more than one phase cycle between two scatterers, or [3] too much perturbation (ε or α terms in Eq. (2)) appears between two scatterers. One way to estimate unwrapping errors is to add a phase unwrapping error in Eq. (2),

$$\Delta\Psi_k(x,y) = \frac{4\pi}{\lambda}\left\{v(x,y)(t_i-t_j)+\frac{1}{2}a(x,y)\left(t_i^2-t_j^2\right)+\frac{1}{6}\Delta a(x,y)\left(t_i^3-t_j^3\right)+\left[D_i(x,y)-D_j(x,y)\right]\right\}+\frac{4\pi}{\lambda}\frac{B_{perp,k}}{R_{x,y}\sin\theta_{x,y}}\Delta h(x,y)+\left[\varepsilon_i(x,y)-\varepsilon_j(x,y)\right]+2\pi L_k(x,y))+\alpha_k(x,y) \quad (11)$$

where L_k represents the cycle(s) of unwrapping error in the k-interferogram, so L_k is an integer. L_k can be estimated by minimizing total model fitting error $\alpha_k(x,y)$. Therefore, we can modify the phase term $\Delta\Psi_k(x,y)$ and iterate Eq. (11) until $L_k = 0$. However, this estimation is solely based on minimizing model fitting errors, and it could overestimate the unwrapping cycles (L_k) and hence underestimate the deformation terms (v, a, Δa). As a result, we only iterate this process once for estimating L_k.

From the mean LOS velocity map of the ERS dataset (Fig. 3a), we find velocity discontinuity between image frames, especially in Changhua County and north of the Pingtung town (regions marked in red circles in Fig. 3a). These two areas do not have high density of point scatterers because the lands are mainly agriculture used, and therefore the distance between scatterers are relatively longer and could cause phase unwrapping error especially in frame 3123. Phase unwrapping becomes even more challenging in areas with sparse point scatterers when the actual subsidence rates are very high. This is because deformation between two scatterers may be more than one phase cycle (2.8 cm for C-band ERS and Envisat), and therefore minimizing residual in Eq. (11) would lead to underestimation of v, a, and Δa terms, which represent real deformation.

The spatial phase unwrapping is less of an issue for the Envisat dataset, because it is a continuous frame and the coherence in interferograms is generally higher than for the ERS dataset. However, the first two acquisitions in 2005 are more than one year away from the third acquisition, and therefore for areas with higher background velocity there could be a higher chance of phase wrapping errors. For example, in Changhua (Fig. 6b) the InSAR time series underestimates the long-term mean velocity ($\bar{v}$ in Eq. (6)) due to a one-year acquisition gap and higher background velocity (~3 cm at FUNY GPS station). This underestimate is also seen in another CGPS site VR02 (dark blue circle in Fig. 5b) in Changhua County.

To summarize, imposing an additional phase unwrapping error term (L_k in Eq. (11)) could potentially detect unwrapping error, but it could possibly underestimate the long-term velocity because the algorithm is based on minimizing model fitting misfit. We find that in areas with higher point scatterer density with dense and continuous acquisitions, phase unwrapping error can be significantly reduced even in a region with higher long-term velocity.

Please cite this article as: Huang, M.-H., et al., Fifteen years of surface deformation in Western Taiwan: Insight from SAR interferometry, Tectonophysics (2016), http://dx.doi.org/10.1016/j.tecto.2016.02.021

6.2. Seasonal precipitation and land subsidence in western Taiwan

Fig. 4 highlights the amplitude of seasonality in western Taiwan, and Figs. 6 and 7 show examples of time series with seasonal variation in time. Here we compare the time series with precipitation data in order to find the correlation between both. We select rain gauge data from the Central Weather Bureau (http://www.cwb.gov.tw) during 2005–2008. To compare precipitation and surface displacement, we select point scatterers close to selected CGPS stations that have higher seasonality. To highlight seasonality, we remove the long-term LOS velocity from the original InSAR or GPS time series (Fig. 8).

This result (Fig. 8) shows some correlation between surface deformation and precipitation with a time delay, especially for sites in Yunlin, Chiayi, and Pingtung. In Yunlin, Chiayi, and Pingtung areas, both InSAR and CGPS indicate rapid uplift following by slower subsidence, and this pattern is different from monthly precipitation time series. This behavior is similar to some time series of groundwater table in central Taiwan (Liu et al., 2004), which may reflect a rapid increase of hydraulic head due to surface water (e.g. rain) infiltration and a more stable discharge due to anthropogenic groundwater pumping.

The time delay between surface deformation and precipitation in Fig. 8 shows an ~4 months lag in Yunlin (TKJS), ~3.5 months in Chiayi (PKGM), ~2 months in Kaohsiung (KASH), and ~3 months in Pingtung (NJOU), whereas there is no significant time delay in Changhua (CHSG) and Tainan (GS34) (see Fig. 3b for location of the CGPS stations). The time delay indicates a different hydraulic conductivity in different regions in western Taiwan and may imply change of a different aquifer system and a different sediment property in the Western Plain. However, we do not have a complete set of groundwater well time series data to further investigate relationships between surface deformation and hydraulic head change. By incorporating with hydraulic level and precipitation time series data, we will be able to estimate storativity and hydraulic conductivity in the sedimentary layers, which is important for groundwater monitoring and management.

6.3. Tectonic deformation in western Taiwan

Tectonic surface deformation in western Taiwan is mainly associated with secular interseismic motion and co- and post-seismic deformations. The main challenge to discriminate tectonic signals from hydrological deformation is that both contributions may have the similar amplitudes and spatial patterns. The seasonal hydrologic deformation is related to time dependent sources such as annual precipitation, groundwater table changes, or seasonal anthropogenic water pumping. This phenomenon is different from longer-term tectonic deformation such as interseismic elastic strain accumulation or aseismic creep along faults. As a result, we consider the seasonal surface variation (Fig. 4) as an indicator to discriminate short-term (seasonal and hydrological) from long-term (tectonic) deformation. Indeed, continuous pumping from an aquifer could reduce water pressure and therefore lead to more continuous subsidence. This process is non-periodic and cannot be recovered in a short time period, but annual discharge (pumping) and recharge (precipitation) of groundwater at the same location would also contribute seasonal subsidence and uplift such as that shown in Fig. 8. This result implies that areas with steady state land subsidence are also likely to have higher seasonal amplitude, which is seen in west coastal area in Figs. 3 and 4. As a result, in this study we separate tectonic and hydrologic contributions based on amplitude of seasonal variation (Fig. 4), so the longer-term (decadal) deformation is considered as dominant due to tectonics.

In both 1995–2001 and 2005–2008 time periods, there is higher surface uplift near the Meishan fault with ~8 mm/yr uplift during 1996–2001 and ~5 mm/yr during 2005–2008, and near the Tsocheng–Hsinhua faults with ~5 mm/yr during 1996–2001 and ~10 mm/yr during 2005–2008 (Fig. 3). The seismicity in western Taiwan (Fig. 1a) shows a shallow (<10 km) seismicity between the Meishan and the Tsocheng faults. The two high surface uplift regions locate roughly at the northern and southern ends of this area of shallow (0–10 km depth; Fig. 1a) seismicity. The source of the seismicity and surface uplift

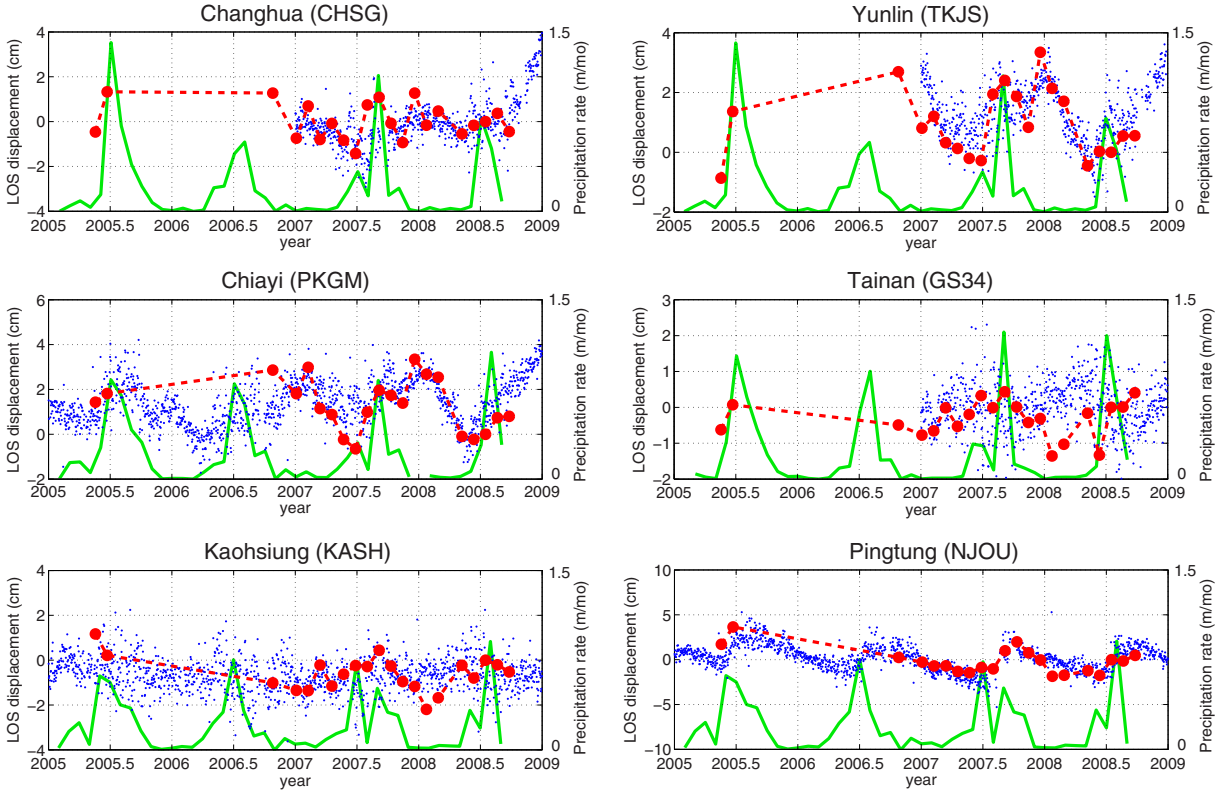

Fig. 8. Comparison of InSAR (red dots), GPS (blue dots), and precipitation data (green lines). Note that the long-term InSAR and GPS mean LOS velocities are removed. See Fig. 3b for locations. (For interpretation of the references to color in this figure legend, the reader is referred to the online version of this chapter.)

Please cite this article as: Huang, M.-H., et al., Fifteen years of surface deformation in Western Taiwan: Insight from SAR interferometry, Tectonophysics (2016), http://dx.doi.org/10.1016/j.tecto.2016.02.021

might be related, but the understanding of the deformation mechanism requires more detailed seismic and structural data to constrain regional structures. Nevertheless, it is clear that the pattern of uplift is different from horizontal deformation revealed from CGPS (Fig. 1c) and is not correlated with horizontal strain rate pattern (Lin et al., 2010; Ching et al., 2011).

In the Pingtung Plain, the range increase (blue region in Fig. 3) is mainly the result of southwestward horizontal displacement (Fig. 1a) due to tectonic escape (Hu et al., 2007; Lin et al., 2010; Ching et al., 2011). On a regional scale, there is surface creep across the left-lateral sense strike-slip Fengshan fault. The surface creep of this fault was not clear from GPS measurements (Fig. 1c; also see Hu et al., 2007) due to sparse station distribution, and is confirmed by this study.

7. Conclusion

We investigate crustal deformation in western Taiwan during 1995–2001 and 2005–2008 using InSAR and CGPS time series. Our results reveal regions with a satellite range increase including coastal Changhua, Yunlin, Chiayi, and southern Pingtung counties due to land subsidence, and the Pingtung Plain due to tectonic escape. Most of the land subsidence areas are coupled with substantial (>10 mm) seasonal deformation that can be separated from tectonic deformation. Near the Meishan fault in the Chiayi County, tectonic surface uplift and the regional shallow (<10 km) seismicity might be related to the same tectonic structure. In the Tainan tableland, a pop-up or back thrust structure could explain crustal uplift in the tableland. East of the tableland there is a change of surface movement from subsidence during 1996–2001 to uplift during 2005–2008. Mean LOS velocity and seasonality of western Taiwan revealed by InSAR outline anthropogenic water usage and tectonic deformation, which are important topics for land usage and hazard monitoring. Our results illustrate the ability of InSAR to reveal spatio-temporal crustal deformation with high density of spatial coverage and accuracy. Investigating fault locking depth and slip in interseismic and coseismic periods from surface deformation observation will help estimate slip budget and thus benefits natural hazard mitigation.

Acknowledgments

The authors would like to thank John Suppe, Maryline Le Béon, Ya-Ju Hsu, and Estelle Chaussard for discussions that significantly improved the manuscript. Three anonymous reviewers and the associate editor provide critical reviews and comments that significantly improved the manuscript. The Larsen fellowship and NASA grant NNX12AQ32G supported M.-H. Huang for this study, and M.-H. Huang is currently supported by an appointment to the NASA Postdoctoral Program at the Jet Propulsion Laboratory, administered by Oak Ridge Associated Universities through a contract with NASA. The research was carried out at the Jet Propulsion Laboratory, California Institute of Technology, under a contract with the National Aeronautics and Space Administration. The ERS SAR images were purchased under NSC 98-2628-M-002-016 and NSC 101-2116-M-002-012, and the Envisat ASAR images are available through ESA project number 28610. Other precipitation data are available at the Center Weather Bureau, Taiwan website (http://www.cwb.gov.tw). The seismicity data are downloaded from the Taiwan Earthquake Center (http://tec.earth.sinica.edu.tw). The continuous GPS time series data are downloaded from the GPS laboratory at the Institute of Earth Science, Academia Sinica, Taiwan (http://gps.earth.sinica.edu.tw). This is BSL contribution #2016-01.

References

Avouac, J.-P., 2015. Seismic and aseismic fault slip to dynamic modeling of the seismic cycle. Annu. Rev. Earth Planet. Sci. 43, 233–271. http://dx.doi.org/10.1146/annurev-earth-060614-105302.

Berardino, P., Fornaro, G., Lanari, R., Sansosti, E., 2002. A new algorithm for surface deformation monitoring based on small baseline differential SAR interferograms. IEEE Trans. Geosci. Remote Sens. 40, 2375–2383.

Bürgmann, R., Rosen, P.A., Fielding, E.J., 2000. Synthetic aperture radar interferometry to measure Earth's surface topography and its deformation. Annu. Rev. Earth Planet. Sci. 28, 169–209.

Carena, S., Suppe, J., Kao, H., 2002. Active detachment of Taiwan illuminated by small earthquakes and its control of first-order topography. Geology 10, 935–938.

Chang, C.-P., Wang, C.-T., Chang, T.-Y., Chen, K.-S., Liang, L.-S., Pathier, E., Angelier, J., 2004. Application of SAR interferometry to a large thrust deformation: the 1999 $M_w = 7.6$ Chichi earthquake in central Taiwan. Geophys. J. Int. 159, 9–16.

Chaussard, E., Bürgmann, R., Shirzaei, M., Fielding, E.J., Baker, B., 2014. Predictability of hydraulic head changes and characterization of aquifer-system and fault properties from InSAR-derived ground deformation. J. Geophys. Res. 119, 6572–6590.

Chen, Y.-G., Liu, T.-K., 2000. Holocene uplift and subsidence along an active tectonic margin southwestern Taiwan. Quat. Sci. Rev. 19, 923–930.

Chen, C.W., Zebker, H.A., 2002. Phase unwrapping for large SAR interferograms: statistical segmentation and generalized network models. IEEE Trans. Geosci. Resmote Sens. 40 (8), 1709–1719.

Chen, C.-T., Hu, J.-C., Lu, C.-Y., Lee, J.-C., Chan, Y.-C., 2007. Thirty-year land elevation change from subsidence to uplift flowing the termination of groundwater pumping and its geological implications in the Metropolitan Taipei Basin, Northern Taiwan. Eng. Geol. 95, 30–47.

Chen, K.-H., Yang, M., Huang, Y.-T., Ching, K.-E., Rau, R.-J., 2011. Vertical displacement rate field of Taiwan from geodetic leveling data 2000–2008. Surv. Rev. 43, 296–302.

Ching, K.-E., Rau, R.-J., Lee, J.-C., Hu, J.-C., 2007. Contemporary deformation of tectonic escape in SW Taiwan from GPS observations, 1995–2005. Earth Planet. Sci. Lett. 262, 601–619.

Ching, K.-E., Rau, R.-J., Johnson, K.M., Lee, J.-C., Hu, J.-C., 2011. Present-day kinematics of active mountain building in Taiwan from GPS observations during 1995–2005. J. Geophys. Res. 116, B09405.

Fattahi, H., Amelung, F., 2014. InSAR uncertainty due to orbital errors. Geophys. J. Int. 199, 549–560. http://dx.doi.org/10.1093/gji/ggu276.

Ferretti, A., Prati, C., Rocca, F., 2000. Nonlinear subsidence rate estimation using permanent scatterers in differential SAR interferometry. IEEE Trans. Geosci. Remote Sens. 38, 2202–2212.

Fruneau, B., Pathier, E., Raymond, D., Defffontaines, B., Lee, C.-T., Wang, H.-T., Angelier, J., Rudant, J.-P., Chang, C.-P., 2001. Uplift of Tainan tableland (SW Taiwan) revealed by SAR interferometry. Geophys. Res. Lett. 28, 3071.

Fuller, C.W., Willett, S.D., Fisher, D., Lu, C.-Y., 2006. A thermomechanical wedge model of Taiwan constrained by fission-track thermochronometry. Tectonophysics 425, 1–24. http://dx.doi.org/10.1016/j.tecto.2006.05.018.

Ho, C.-S., 1986. A synthesis of the geological evolution of Taiwan. Tectonophysics 125, 1–16.

Hooper, A., 2008. A multi-temporal InSAR method incorporating both persistent scatterer and small baseline approaches. Geophys. Res. Lett. 35, L16302.

Hsieh, C.-S., Shih, T.-H., Hu, J.-C., Tung, H., Huang, M.-H., Angelier, J., 2011. Using differential SAR interferometry to map land subsidence: a case study in the Pingtung Plain of SW Taiwan. Nat. Hazards 58, 1331–1332.

Hsu, S.-K., 1998. Plan for a ground water monitoring network in Taiwan. Hydrogeol. J. 6, 405–415.

Hsu, Y.-J., Yu, S.-B., Simons, M., Kuo, L.-Ch., Chen, H.-Y., 2009. Interseismic crustal deformation in the Taiwan plate boundary zone revealed by GPS observations, seismicity, and earthquake focal mechanisms. Tectonophysics 479, 4–18.

Hu, J.-C., Chu, H.-T., Hou, C.-S., Lai, T.-H., Chen, R.-F., Nien, P.-F., 2006. The contribution to tectonic subsidence by groundwater abstraction in the Pingtung area, southwestern Taiwan as determined by GPS measurements. Quat. Int. 147, 62–69.

Hu, J.-C., Hou, C.-S., Shen, L.-C., Chan, Y.-C., Chen, R.-F., Huang, C., Rau, R.-J., Chen, K.H.-H., Lin, C.-W., Huang, M.-H., Nien, P.-F., 2007. Fault activity and lateral extrusion inferred from velocity field revealed by GPS measurements in the Pingtung area of southwestern Taiwan. J. Asian Earth Sci. 31, 287–302.

Huang, M.-H., Hu, J.-C., Hsieh, C.-S., Ching, K.-E., Rau, R.-J., Pathier, E., Fruneau, B., Deffontaines, B., 2006. A growing structure near the deformation front in SW Taiwan as deduced from SAR interferometry and geodetic observation. Geophys. Res. Lett. 33, L12305.

Huang, M.-H., Hu, J.-C., Ching, K.-E., Rau, R.-J., Hsieh, C.-S., Pathier, E., Fruneau, B., Deffontaines, B., 2009. Active deformation of Tainan tableland of southwestern Taiwan based on geodetic measurements and SAR interferometry. Tectonophysics 466, 322–334.

Huang, M.-H., Dreger, D., Bürgmann, R., Yoo, S.-H., Hashimoto, M., 2013. Joint inversion of seismic and geodetic data for the source of the 4th March 2010 Mw 6.3 Jia-Shian, SW Taiwan, earthquake. Geophys. J. Int. 193 (3), 1608–1626.

Hung, W.-C., Hwang, C., Chang, C.-P., Yen, J.-Y., Liu, C.-H., Yang, W.-H., 2010. Monitoring severe aquifer-system compaction and land subsidence in Taiwan using multiple sensors: Yunlin, the southern Choshui River Alluvial Fan. Environ. Earth Sci. 59, 1535–1548.

Hung, W.-C., Hwang, C., Chen, Y.-A., Chang, C.-P., Yen, J.-Y., Hooper, A., Yang, C.-Y., 2011. Surface deformation from persistent scatterers SAR interferometry and fusion with leveling data: a case study over the Choushui River Alluvial Fan, Taiwan. Remote Sens. Environ. 115, 957–967.

Lacombe, O., Mouthereau, F., Angelier, J., Deffontaines, B., 2001. Structural, geodetic and seismological evidence for tectonic escape in SW Taiwan. Tectonophysics 333, 323–345.

Lin, K.-C., Hu, J.-C., Ching, K.-E., Angelier, J., Rau, R.-J., Yu, S.-B., Tsai, C.-H., Shin, T.-C., Huang, M.-H., 2010. GPS crustal deformation, strain rate, and seismic activity after the 1999 Chi–Chi earthquake in Taiwan. J. Geophys. Res. 115, B07404.

Please cite this article as: Huang, M.-H., et al., Fifteen years of surface deformation in Western Taiwan: Insight from SAR interferometry, Tectonophysics (2016), http://dx.doi.org/10.1016/j.tecto.2016.02.021

Liu, C.-H., Pan, Y.-W., Liao, J.-J., Huang, C.-T., Ouyang, S., 2004. Characterization of land subsidence in the Choshui River alluvial fan, Taiwan. Environ. Geol. 45, 1154–1166.
Marinkovic, P., Larsen, Y., 2013. Consequences of long-term ASAR local oscillator frequency decay — an empirical study of 10 years of data, European Space Agency. Proceedings of the Living Planet Symposium (Abstract), Edinburgh, U.K.
Menke, 1989. Geophysical data analysis: discrete inverse theory 289 pp. Academic Press Inc., Harcourt Brace Jovanovich Publishers, San Diego.
Miller, M.M., Shirzaei, M., 2015. Spatiotemporal characterization of land subsidence and uplift in Phoenix using InSAR time series and wavelet transforms. J. Geophys. Res. 120, 5822–5842. http://dx.doi.org/10.1002/2015JB012017.
Mora, O., Mallorqui, J.J., Broquetas, A., 2003. Linear and nonlinear terrain deformation maps from a reduced set of interferometric SAR images. IEEE Trans. Geosci. Remote Sens. 41, 2243–2253.
Pathier, E., Fruneau, B., Deffontaines, B., Angelier, J., Chang, C.-P., Yu, S.-B., Lee, C.-T., 2003. Coseismic displacements of the footwall of the Chelungpu fault caused by the 1999, Taiwan, Chi–Chi earthquake from InSAR and GPS data. Earth Planet. Sci. Lett. 212, 73–88.
Rosen, R.A., Hensley, S., Pelzer, G., 2004. Updated repeat orbit interferometry package released. EOS, Trans. Am. Geophys. Union 85 (5), 35.
Schmidt, D.A., Bürgmann, R., 2003. Time dependent land uplift and subsidence in the Santa Clara valley, California, from a large InSAR data set. J. Geophys. Res. 108. http://dx.doi.org/10.1029/2002JB002267.
Shyu, J.B.H., Sieh, K., Chen, Y.-G., Liu, C.-S., 2005. Neotectonic architecture of Taiwan and its implications for future large earthquakes. J. Geophys. Res. 110, B08402.
Suppe, J., 1984. Kinematics of arc–continent collision, flipping of subduction and back-arc spreading near Taiwan. Mem. Geol. Soc. China 6, 21–33.
Tung, H., Hu, J.-C., 2012. Assessments of serious anthropogenic land subsidence in Yunlin County of central Taiwan from 1996 to 1999 by persistent scatterers InSAR. Tectonophysics 578, 126–135.
Wu, Y.-Y., Hu, J.-C., Lin, G.-P., Chang, C.-P., Tung, H., Lu, C.-H., 2013. Transient active deformation in Tainan tableland using persistent scatterers SAR interferometry. Bull. Soc. Geol. Fr. 184, 441–450.
Yu, S.-B., Chen, H.-Y., Kuo, L.-C., 1997. Velocity field of GPS stations in the Taiwan area. Tectonophysics 274, 41–59.

Please cite this article as: Huang, M.-H., et al., Fifteen years of surface deformation in Western Taiwan: Insight from SAR interferometry, Tectonophysics (2016), http://dx.doi.org/10.1016/j.tecto.2016.02.021